21 Jun 2014

Curvature Induced Phase Stability of an Intensely Heated Liquid

Kiran Sasikumar

Zhi Liang
Missouri University of Science and Technology, zlch5@mst.edu

David G. Cahill

Pawel Keblinski

Recommended Citation

K. Sasikumar et al., "Curvature Induced Phase Stability of an Intensely Heated Liquid," *Journal of Chemical Physics*, vol. 140, no. 23, article no. 234506, American Institute of Physics, Jun 2014.
The definitive version is available at https://doi.org/10.1063/1.4883516

The Journal of Chemical Physics

Curvature induced phase stability of an intensely heated liquid

Cite as: J. Chem. Phys. **140**, 234506 (2014); https://doi.org/10.1063/1.4883516
Submitted: 23 April 2014 • Accepted: 03 June 2014 • Published Online: 19 June 2014

Kiran Sasikumar, Zhi Liang, David G. Cahill, et al.

AIP Publishing

Curvature induced phase stability of an intensely heated liquid

Kiran Sasikumar,[1,2] Zhi Liang,[2] David G. Cahill,[3] and Pawel Keblinski[1,2,a)]
[1]*Department of Materials Science and Engineering, Rensselaer Polytechnic Institute, Troy, New York 12180, USA*
[2]*Rensselaer Nanotechnology Center, Rensselaer Polytechnic Institute, Troy, New York 12180, USA*
[3]*Department of Materials Science and Engineering, and Materials Research Laboratory, University of Illinois Urbana, Illinois 61801, USA*

(Received 23 April 2014; accepted 3 June 2014; published online 19 June 2014)

We use non-equilibrium molecular dynamics simulations to study the heat transfer around intensely heated solid nanoparticles immersed in a model Lennard-Jones fluid. We focus our studies on the role of the nanoparticle curvature on the liquid phase stability under steady-state heating. For small nanoparticles we observe a stable liquid phase near the nanoparticle surface, which can be at a temperature well above the boiling point. Furthermore, for particles with radius smaller than a critical radius of 2 nm we do not observe formation of vapor even above the critical temperature. Instead, we report the existence of a stable fluid region with a density much larger than that of the vapor phase. We explain the stability in terms of the Laplace pressure associated with the formation of a vapor nanocavity and the associated effect on the Gibbs free energy. © *2014 AIP Publishing LLC*. [http://dx.doi.org/10.1063/1.4883516]

I. INTRODUCTION

A particularly challenging and important aspect of nanoscale heat transfer[1,2] is the problem of the exchange of heat between a solid nanoparticle and the surrounding liquid. This has several important applications, not least, in the field of medicine wherein there is significant ongoing research on the use of nanoparticles for hyperthermia-based destruction of tumor cells.[3–6] Thermal therapeutics offers several benefits over conventional approaches for cancer treatment: they are non-invasive, relatively simple to perform, and have the potential of treating embedded tumors in regions where surgery is difficult.

However, understanding of the thermal transport, the distribution of the temperature field, and associated microstructural changes and phase transformations is limited. Remarkably, several transient laser-heating experiments have observed metal nanoparticle melting without an associated boiling of the surrounding fluid.[7,8] A similar observation has been made in molecular dynamics (MD) simulations that mimic such experiments.[9] This unusual phase stability is not well understood and designing experiments to understand the physics of this phenomenon is a challenging task. Here, we employ MD simulations, which offer a powerful tool to investigate this phenomenon without the simplifying assumptions required by continuum-level model formulations.

Initial work on this topic by Merabia *et al.*[10] demonstrated stability of the liquid around heated nanoparticles even above the critical temperature. The authors hypothesized that the stability is created by the Laplace pressure associated with the formation of a nanoscale vapor sphere with high curvature.[11] However, the boundary conditions were not realistic as the heat sinks maintaining ambient temperature were placed only a few nanometers from nanoparticle surfaces. The unrealistic boundary conditions might have affected the results, e.g., by stabilizing the liquid. In this work, in addition to reproducing the high temperature stability of the liquid we investigate the heat transfer around several nanoparticle sizes and determine the critical particle size above which a standard liquid-to-vapor phase change is observed upon nanoparticle heating.

The first part of our work is on MD simulations of heated nanoparticles in a liquid, in the presence of a self-consistent boundary condition obtained via an iterative procedure that ensures that the temperature field away from the nanoparticle is consistent with the macroscopic heat transfer description (see Sec. II B). In addition, we simulate heat transfer for a range of nanoparticle sizes to investigate the effect of curvature on phase stability and heat transfer. In the second part of our work we estimate the free energy driving the phase change and its relationship with the liquid phase stability.

The paper is organized as follows. Sections II A and II B describe model structures, the MD methodology, and the boundary conditions used to determine the dependence of phase stability on curvature. Section II C discusses techniques used to determine the local pressure in spherically symmetric systems. The results of our non-equilibrium molecular dynamics (NEMD) simulations are presented in Sec. III A, and are followed by an analysis of the free energy in Secs. III B and III C. Finally, the summary and conclusions are presented in Sec. IV.

II. MODEL STRUCTURE AND SIMULATION METHODOLOGY

A. Atomistic model structure

Our model system for MD simulations is argon-like fluid atoms embedding a solid nanoparticle (NP) of varying radii. The schematic of the model system is shown in Fig. 1. The

a)Electronic mail: keblip@rpi.edu

Lennard-Jones (LJ) interatomic potential,[10,12] as described by Eq. (1), is used to describe the force field in the monoatomic fluid:

$$V(r) = 4 \in \left[\left(\frac{\sigma}{r}\right)^{12} - \left(\frac{\sigma}{r}\right)^{6}\right]. \quad (1)$$

Energy, $\in$, and length, σ, parameters are chosen as 0.5758 kcal/mol and 0.3 nm, respectively, to make them consistent with the parameters used by Merabia *et al.* in Ref. 10. The size of the fluid domain is increased, as appropriate, with increasing nanoparticle size, as to ensure a minimum distance from the particle surface to the edge of the simulation cell of 10σ.[10] The smallest simulation involves ~60 000 fluid atoms, while the largest system simulated has ~150 000 atoms.

Solid nanoparticles are inserted in the center of the simulation box. Their radii range from 5 Å to 40 Å. The particles are carved out of a crystal of atoms arranged on the face-centered cubic (FCC) lattice. In addition to the LJ potential, nearest-neighbor solid atoms are held together by finitely extensible nonlinear elastic (FENE) springs.[10] FENE springs permit the solid to be heated to arbitrary high temperatures without melting. The use of FENE springs allows us to investigate extreme heat fluxes and their influence on the fluid. The interaction between the solid and fluid is also described by a LJ force field with the same parameters as used for the fluid-fluid interaction. This case corresponds to a solvophilic solid immersed in the fluid.

B. MD methodology

The model systems are first equilibrated at a constant pressure of 20 atm and a temperature of 200 K for 2.5 ns using a Nose-Hoover thermostat and barostat. At 20 atm, the boiling point of our system is ~243 K (see Sec. III B) and the limit of superheat or the mechanical boiling point[13,14] is ~310 K (refer to Sec. III B). The superheat limit corresponds to the situation where the compressibility of the bulk liquid becomes negative and, consequently, the liquid becomes unstable with no nucleation barrier for vaporization.[13]

After equilibration, we perform NEMD simulations to establish a heat flux through the system. A Nose-Hoover barostat is used to maintain constant ambient pressure of 20 atm. The whole nanoparticle is a heat source and is kept at high and constant temperature in the 220 K–3000 K range via velocity rescaling. The heat sink is placed in a spherically symmetric shell centered with the nanoparticle. To mimic embedding of the nanoparticle in a large liquid volume, the temperature of the heat sink is established interactively as to follow the temperature field characterizing a spherically symmetric heat source (see Fig. 1):

$$T_{sink} = T_{\infty} + \frac{Q}{4\pi k r_{sink}}, \quad (2)$$

where T is the temperature, Q is the heat power, k is the thermal conductivity of the fluid, and r is the radial distance. The ambient temperature, T_{∞}, is 200 K. A constant thermal conductivity of 0.2 W/m-K (estimated from independent MD simulations of a bulk fluid system at a pressure of 20 atm and temperatures varying between 200 K and 250 K) is assumed while establishing the sink temperature.

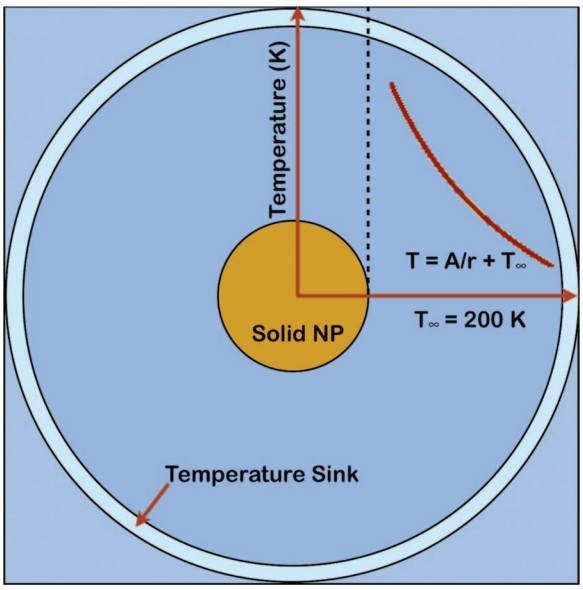

FIG. 1. System schematic depicting the central nanoparticle, surrounding fluid, and the location of the temperature sink.

However, we do not know the value of the power of the heat source at the start of the simulation. For this purpose, we use an iterative scheme that determines a self-consistent temperature at the boundary. During the first iteration we impose the sink temperature to be 200 K, i.e., ambient temperature. Once the steady state is established, we evaluate the heat power (Q) based on the changes in energy of the system upon velocity rescaling. Then, via Eq. (2) a new sink temperature, T_{sink}, is calculated for the next iteration. Typically, 4-5 iterations are needed such that the total system energy, sink temperature, and the heat flux flowing through the system stabilize to a constant value within reasonable error bars. For the largest heating fluxes the sink temperature computed by this scheme stabilizes to ~235 K after 4-5 iterations.

C. Calculation of local pressures

The average pressure tensor, $\boldsymbol{P}$, over the entire simulation box is calculated using the virial formula,[15]

$$\boldsymbol{P}_{\beta\alpha} = \frac{1}{V}\left[\sum_{i=1}^{N}\left(m_i v_{i\beta} v_{i\alpha} + f_{i\beta} r_{i\alpha}\right)\right], \quad (3)$$

where β and α correspond to the x, y, or z coordinate, m_i is the mass of the ith atom, $v_{i\beta}$ is the β velocity component of atom i, $f_{i\beta}$ is the β component of the total force on atom i, and $r_{i\alpha}$ is the α projection of the atom position. N is the total number of atoms in the simulation box and V is the box volume.

However, there is an ambiguity in defining the local pressure tensor, particularly for non-homogeneous structures. This was pointed out by Irving and Kirkwood[16] and arises from the arbitrary choice of non-local particle interactions that contribute to the local force. By restricting the summation in Eq. (3) to the atoms in a spherical shell around the nanoparticle and replacing the box volume, V, with the volume of the shell, we can calculate the local hydrostatic pressure. This is

called the IK-1 approximation[17] as it is the zeroth order approximation of the Irving Kirkwood (IK) expression for the local pressure tensor.[16,17] As discussed in Refs. 16 and 18, the IK-1 approximation is inappropriate for heterogeneous systems and the density variation in the liquid near the nanoparticle surface induced by a high temperature gradient[10] results in erroneous estimation of the local pressure in the vicinity of the nanoparticle.

Several techniques have been developed to calculate the local pressure tensor for heterogenous systems such as those of IK[16,18] and Harasima.[18,19] The normal component of the pressure tensor $\boldsymbol{P}_N$ can be unambiguously obtained independent of the calculation technique.[18] The authors of Ref. 18 derive a simplified IK expression for the pressure acting perpendicular to the polymer film boundary (Eq. (11) in Ref. 18). We modify this equation for application in spherically symmetric systems and calculate $\boldsymbol{P}_N(r) = \boldsymbol{P}_{rr}(r)$:

$$\boldsymbol{P}_{rr}(r) = \rho(r) k_B T(r) + \frac{1}{8\pi r^2} \sum_{i=1}^{N} \sum_{i \neq j} f_{r,ij}(r_{ij}) \Theta\left(\frac{r - r_i}{r_{ij}}\right) \Theta\left(\frac{r_j - r}{r_{ij}}\right), \tag{4}$$

where $\rho(r)$ is the local density and $T(r)$ is the local temperature in a spherical shell of radius r and thickness Δr taken to be large enough to obtain adequate statistical averaging. k_B is the Boltzmann constant, $f_{r,ij}$ is the two-body force in the radial direction, r_i is the radial coordinate of atom i, r_j is the radial coordinate of atom j, and r_{ij} is the distance between atoms i and j. Θ is the Heaviside step function.

However, the validity of this simplified IK expression in non-equilibrium systems has not been verified. Todd *et al.*[17] developed an alternative to the IK expression called the "method of planes" (MOP) based on the mass and momentum continuity equations of hydrodynamics, which like the generalized IK expression, is applicable under non-equilibrium conditions. A similar derivation can be done for spherical systems by employing spherical Hankel transforms.[20,21] We derive the "method of spheres" (MOS) expression for the potential part of the normal pressure using the same routine detailed in Refs. 17 and 22:

$$\boldsymbol{P}^{U}_{rr}(r) = \frac{1}{16\pi r^2} \sum_{i=1}^{N} \sum_{i \neq j} f_{r,ij}(r_{ij}) \times [\Theta(r_i - r)\Theta(r - r_j) - \Theta(r_j - r)\Theta(r - r_i)]. \tag{5}$$

Equation (5) and the potential part of Eq. (4) are essentially identical. Hence, the simplified IK expression for the normal pressure component can be used in non-equilibrium systems. For improved statistics, we employ the volume-average method to calculate $\boldsymbol{P}_{rr}(r)$, which has been shown to be equivalent to MOP.[15] For the spherical system the volume-average expression is

$$\boldsymbol{P}_{rr}(r) = \frac{1}{\Omega}\left(\sum_{i=1}^{N} m_i v_{r,i} v_{r,i} \Lambda_i + \frac{1}{2} \sum_{i=1}^{N} \sum_{i \neq j} f_{r,ij}(r) r_{ij} l_{ij} \right), \tag{6}$$

where Ω is the shell volume, m_i is the mass of the ith atom, $v_{r,i}$ is the radial velocity component of atom i, $f_{r,ij}$ is the radial component of the two-body force between atoms i and j, l_{ij} is the fraction of r_{ij} that lies within the spherical shell, and Λ_i is 1 if atom i lies in the averaging volume Ω; otherwise, it is 0.

III. RESULTS AND DISCUSSION

A. MD simulation

Temperature, density, and pressure profiles are calculated for structures subjected to a steady-state heat flow with self-consistent boundary conditions. The actual profiles represent averages over ~2.5 ns. The profiles for a 10 Å radius nanoparticle are shown in Fig. 2. For low nanoparticle temperatures, the density profiles (Fig. 2(b)) reveal an ordering of the liquid

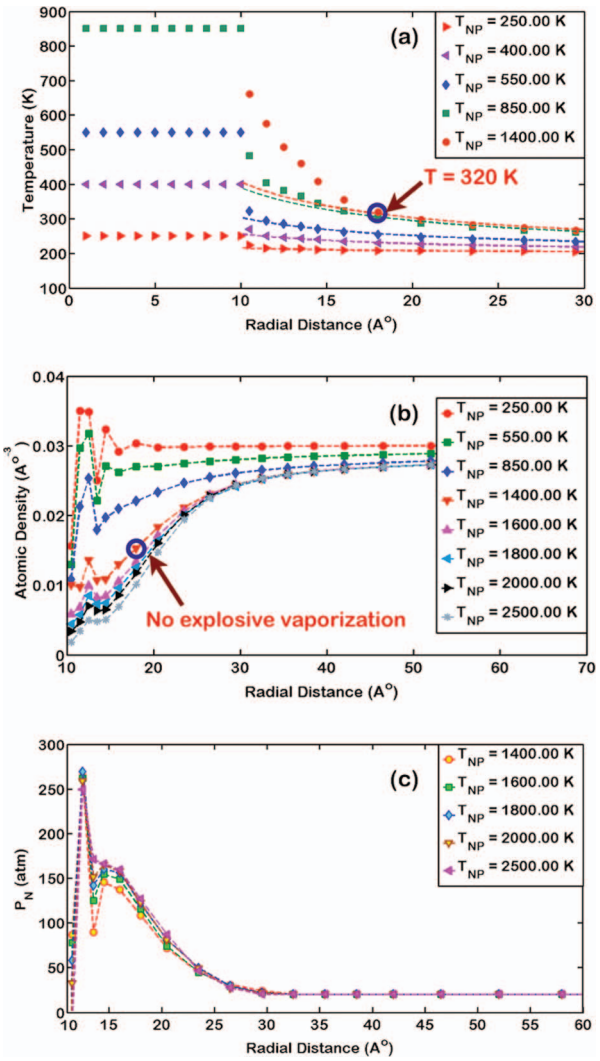

FIG. 2. The steady state profiles around a 10 Å nanoparticle for different particle temperatures. (a) Temperature profile. The dotted lines correspond to a fit based on $T(r) = A/r + B$ which is obtained from continuum heat transfer considerations. (b) The steady state fluid density profiles. The dotted lines are plotted as a visual guide. For the same temperature point marked in (a) it is evident that no explosive vaporization occurs even though the temperature is greater than the mechanical boiling point of 310 K. (c) Pressure profile. The dotted lines are plotted as a visual guide. For all cases, the errors lie within the symbol size.

near the solid surface. This ordering dies out as the temperature of the nanoparticle is increased.

The most striking result, however, is that in some cases the local temperatures in the liquid are above the superheating limit[13] of 310 K. One of the cases is explicitly marked in Fig. 2(a). The bulk liquid at a temperature above 310 K and a pressure of 20 atm is mechanically unstable and vaporizes explosively.[13] We confirmed this in independent simulations of bulk LJ liquid (see Sec. III B). For the system under investigation, an explosive vaporization results in rapid and unconstrained increase of the simulation box volume.[23] At these high temperatures the steady state local density is low, but several times larger than the saturated vapor atomic density of 0.0005 $Å^{-3}$ (see Fig. 2(b)).

The spatial variation of the radial component of the pressure for the high temperature cases is shown in Fig. 2(c). Away from the nanoparticle surface the pressure is equivalent to the ambient pressure of 20 atm. Closer to the nanoparticle surface we observe a significant increase in the normal pressure. This increase is associated with the Laplace-like pressure originating from the density gradient near the nanoparticle surface. However, immediately adjacent to the surface we observe local fluctuations in the pressure data that originates from the ordering or density fluctuation of the fluid. The ordering seen in the density profiles is significant because the chosen solid-fluid interaction is solvophilic in nature.[10] Thus, we consider the ordered shell around the nanoparticles to be the wetting region.

Figure 3 shows the variation of the heat flux flowing from the nanoparticle to the surrounding fluid with increasing nanoparticle temperatures and for different nanoparticle radii. For small nanoparticle temperatures and for all nanoparticle sizes the heat flux varies linearly with the particle temperature. With increasing nanoparticle temperature the heat flux saturates for radii less than 20 Å. For the 15 Å nanoparticle the heat flux saturates at $\sim 20\,GW/m^2$. Furthermore, beyond a critical size of 20 Å the heat flux response is similar to a flat plate in pool boiling heat transfer.[10,24] Here, once the critical heat flux is reached vaporization (de-wetting) occurs, associated with a dramatic drop in the heat flux flowing from the particle to the fluid. The critical heat flux decreases with increasing nanoparticle size.

Figure 2(a) indicates a significant temperature drop at the interface of the solid and the surrounding liquid. This temperature jump is due to the existence of a finite interfacial resistance known as the Kapitza resistance.[25] This interfacial resistance, R, is quantified as

$$R = \frac{\Delta T}{q}, \tag{7}$$

where q is the heat flux flowing through the system and ΔT is the discontinuous temperature drop. The importance of the interfacial resistance can be most easily gauged via a concept of the Kapitza length, i.e., the equivalent thickness of a bulk material forming the interface that has the same overall thermal resistance as the interface. Interfacial effects will be important when the characteristic length-scale of the system – e.g., the diameter of nanoparticle or a layer thickness – is comparable to, or smaller than, the Kapitza length.

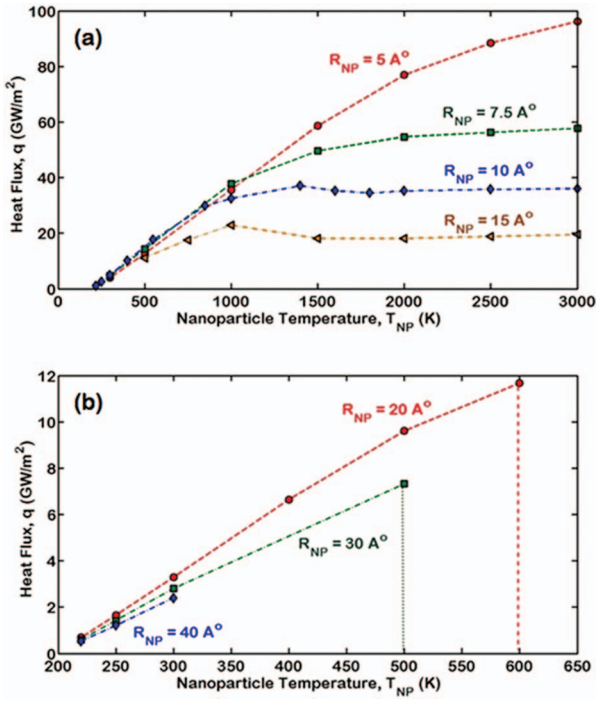

FIG. 3. Variation of the heat flux flowing from the nanoparticle to the surrounding fluid with increasing nanoparticle temperature. The plots are made for several nanoparticle sizes: (a) 5 Å to 15 Å, (b) 20 Å to 40 Å. As the nanoparticle radius increases the critical heat flux decreases. Furthermore, at a critical radius of 20 Å the heat transfer response undergoes a drastic change. While the heat flux flattened out for radii less than the critical radius indicating the formation of a low-density fluid layer, we see vaporization for larger radii due to which there is a sudden drop in the heat flux. The de-wetting point for the 40 Å case was not explored but is expected to occur below a nanoparticle temperature of 500 K. The vertical dotted line represents this drop. The dotted lines between points are plotted as a visual guide. The error in the heat flux estimation lie within the symbol size.

At low nanoparticle temperatures, the fluid temperatures show a good fit to the $T(r) = A/r + B$ form expected from continuum consideration of a steady-state temperature field. This is evident from the dotted lines in Fig. 2(a). As the nanoparticle temperature is increased, a significant departure from the fit is seen. In this context we define two components to the interface resistance as shown for a sample temperature profile in Fig. 4(a). One is the direct interface resistance that is associated with the observed drop across the solid-fluid interface and the second is a resistance associated with the departure from the fit, i.e., an additional resistance associated with hot liquid in the interfacial region. From the temperature drop, ΔT_1, the direct interface resistance, R_1, is calculated using Eq. (7). Similarly using the temperature drop through the interface liquid, ΔT_2, the resistance, R_2, is calculated. This additional resistance is attributed to the existence of the low-density fluid layer near the nanoparticle surface for large surface temperatures; and we call it the nonlinear resistance.

In Fig. 4(b) we plot both interface resistances as a function of nanoparticle temperature for the case of the 10 Å radius nanoparticle. For low nanoparticle temperatures, the overall interface resistance is 0.014 m^2K/MW. This value is similar to the interface resistances of other solvophilic surfaces.[26] For low particle temperatures the nonlinear resistance is zero and starts to increase when the particle

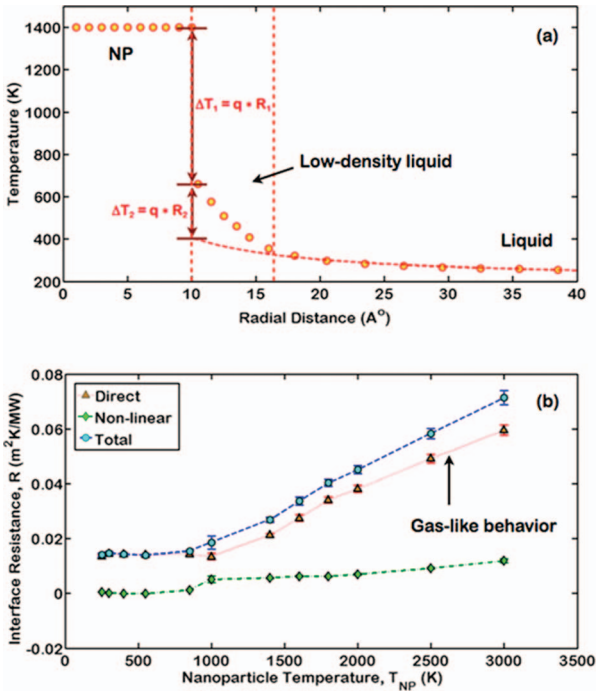

FIG. 4. (a) Sample temperature profile around a 10 Å NP maintained at 1400 K. The dotted line is the fit of the fluid temperature away from the NP surface to $T(r) = A/r + B$. The overall thermal interface resistance around the nanoparticle is split into two components, the direct interface resistance and the nonlinear resistance. From the real or observed temperature drop, ΔT_1, the direct interface resistance, R_1, is calculated using Eq. (7). Similarly, using the temperature drop through the low-density interface fluid, ΔT_2, the nonlinear resistance, R_2, is calculated. Note that q is the heat flux flowing from the solid nanoparticle to the surrounding fluid. (b) Direct, R_1, nonlinear, R_2, and the total interface resistance are plotted as a function of the nanoparticle temperature. The dotted lines between points are plotted as a visual guide. The nonlinear resistance is zero for low nanoparticle temperatures, while it jumps to a finite value at $T_{NP} = 1000$ K for the above representative case of the 10 Å radius nanoparticle. Above this temperature the direct interface resistance also demonstrates a linear variation, which indicates a gas-like behavior of the low-density fluid layer. This is in spite of a fluid density that is at least twice the saturated vapor density for the LJ system being modeled.

temperature exceeds 1000 K. The heat flux saturation for the 10 Å nanoparticle also occurs at a particle temperature of 1000 K (see Fig. 3(a)).

The temperature dependence of the direct interfacial resistance is also interesting (see Fig. 4(b)). This resistance is constant up to the formation of the low-density fluid. For temperatures beyond 1000 K, the direct resistance increases with increasing particle temperature. This increase is characteristic of gases in contact with hot solid surfaces[27,28] and is associated with decreasing gas density. In Fig. 5, we plot the direct interface conductance versus the product of the fluid density and the square root of the fluid temperature, which is associated with the gas atom collision frequency with the solid surface. The linear dependence in Fig. 5 demonstrates behavior characteristic of the gas-solid interfacial heat transfer.[29] Thus, the low-density fluid is, in fact, gas-like in spite being denser than the equilibrium vapor at the same temperature and pressure.

In Fig. 6 we plot the surface fluid temperature at which gas-like behavior starts versus the nanoparticle curvature. The gas-like behavior is either due to the presence of low-density

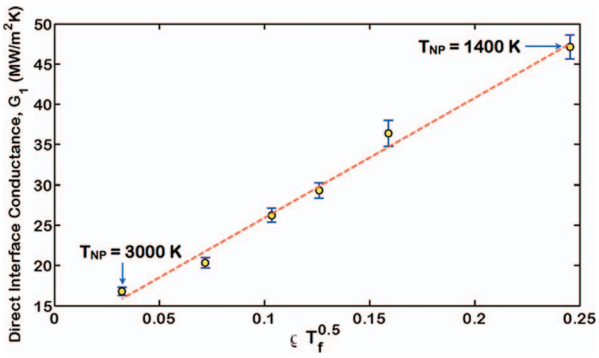

FIG. 5. The direct interface conductance (inverse of the resistance in Fig. 4) is plotted here as a function of the product of the fluid density and the square root of the fluid temperature. The dotted line plots the linear fit. Such a linear variation is characteristic of gases in contact with a solid.[27–29]

fluid layer for nanoparticles smaller than 20 Å in radius or due to explicit phase change de-wetting for larger nanoparticles. We call this temperature the de-wetting temperature and according to Fig. 6 this temperature increases linearly with the curvature. In other words as the nanoparticle size is decreased the surrounding liquid can be heated up to a larger temperature before it undergoes a significant density change.

Extrapolating the linear fit to zero curvature gives a value of 318 ± 7 K. This is close to the mechanical boiling point of 310 K, which is the upper limit for a metastable liquid above the thermodynamic boiling point. Furthermore, the critical temperature of the fluid demarcates the 15 Å and 20 Å nanoparticle sizes. This may explain the observation of the critical size. For nanoparticles smaller than the critical size one observes the formation of the gas-like low-density fluid and for larger particles we see vapor formation as demarcated in Fig. 6.

In Fig. 7 we plot the peak pressure outside the wetting region for all the simulated NP sizes and temperatures. The pressure does not exceed the critical pressure of the fluid for all cases. Hence, the low-density fluid that is seen around the highly curved NPs is not supercritical fluid and exists only in such highly non-equilibrium and non-homogeneous systems.

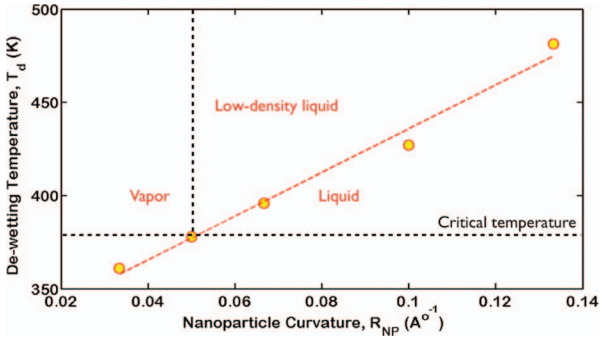

FIG. 6. (Circles) The lowest fluid temperature near the nanoparticle surface at which gas-like behavior is demonstrated in the MD simulations is plotted here versus the nanoparticle curvature. Gas-like behavior exists either due to the low-density fluid layer or due to vaporization around the particle. The corresponding dotted line plots the linear fit. The intercept at zero curvature is 318 ± 7 K, which is close to the mechanical boiling point of the system.

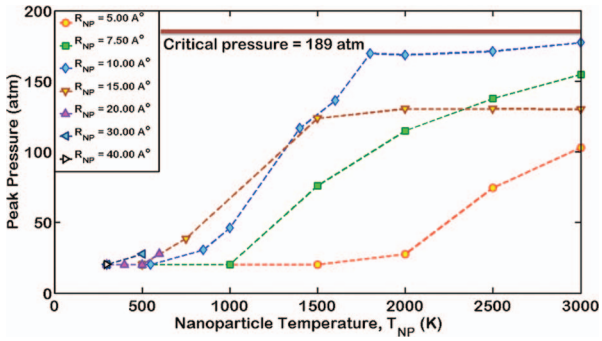

FIG. 7. The peak pressure seen in the fluid for all the simulated nanoparticle temperatures and sizes. The pressure does not exceed critical for all cases. Hence, the low-density phase seen around the hot nanoparticle is not supercritical fluid. The dotted lines between points are plotted as a visual guide.

In Ref. 10 Merabia *et al.* considers that it is the Laplace pressure effect[11] that blocks the formation of a vapor layer around spherical nanoparticles. Consistently, we observe an increase in the local pressure in the vicinity of the NP maintained at very high temperatures (see Fig. 2(c)). In Fig. 8 we plot the surface fluid temperature and the temperature outside the wetting region versus the peak pressure for all the simulated cases where vapor formation is not observed. We see that the local temperatures exceed the boiling point at the corresponding pressures for several cases. This counters the simplistic explanation that the increased boiling point associated with the higher pressure near the surface fully explains the observed suppression of vapor formation. However, an additional consequence of the increased pressure is that it stabilizes the liquid by lowering the driving force for the phase change. In Sec. III C we analyze observed de-wetting temperature enhancements using a free energy based model.

B. Bulk and surface energies

The Gibbs free energy difference between the bulk liquid phase and the vapor phase of the LJ fluid, Δg, is required to calculate the driving force for vaporization. For this purpose, we consider a model system consisting of 13 500 Lennard-Jones atoms in a cubic box with periodic boundaries. The parameters for the fluid are the same as described in Sec. II A. MD simulations are performed on the system at a constant pressure. Once the system is equilibrated to a starting temperature of 230 K at the desired pressure, we evaluate the specific enthalpy, h, of the fluid by gradually heating the fluid to 375 K and then cooling the fluid back down to 230 K. The gradual heating/cooling is done over 20 ns with a time step of 5 fs. Energy and system volume values averaged over 100 ps blocks are used to evaluate the enthalpy variation during the heating and cooling runs. In Fig. 9(a) we plot the specific enthalpy computed for the 50 atm case. Similar to the results reported for argon in Ref. 30, due to nucleation barriers, we see that the vaporization of the bulk liquid occurs at a temperature higher

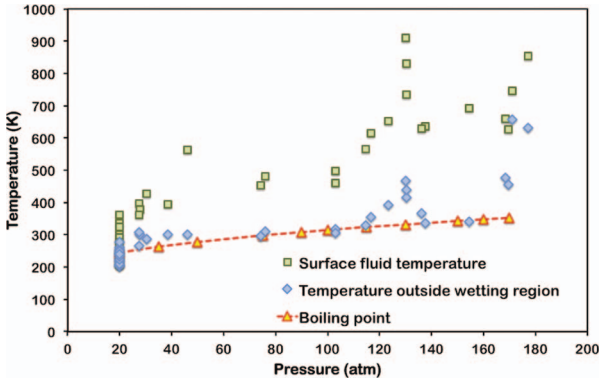

FIG. 8. The surface fluid temperature and the temperature outside the wetting region versus the peak pressure seen in the fluid for all the simulated nanoparticle temperatures and sizes where vapor formation did not occur. The boiling point versus pressure is also plotted. The dotted lines between points are plotted as a visual guide. For some cases local temperatures exceed the boiling point. However, we do not observe vaporization for these cases.

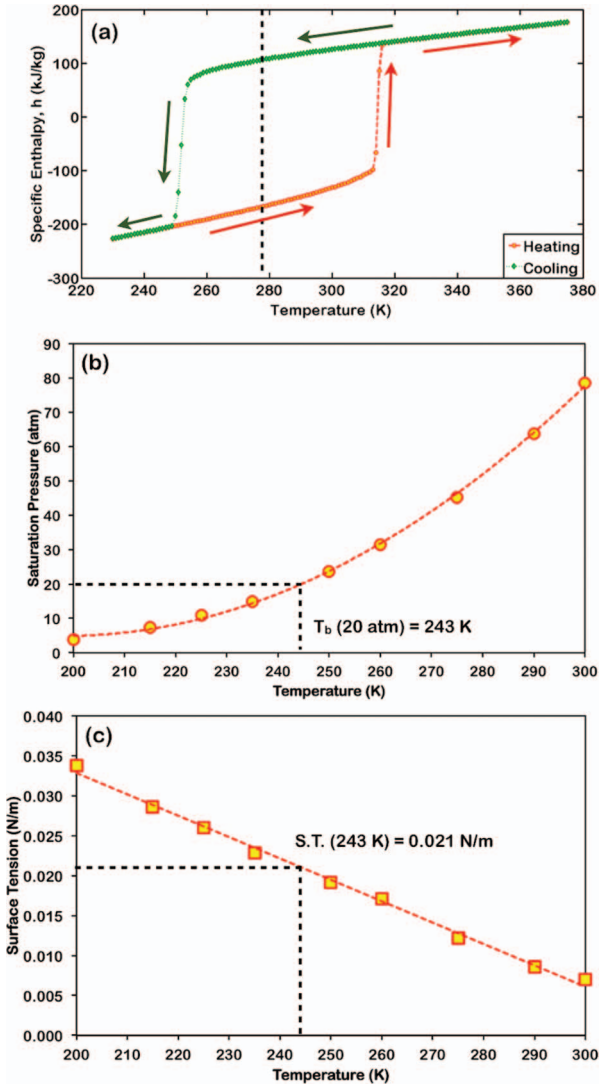

FIG. 9. (a) Specific enthalpies obtained for a bulk fluid maintained at 50 atm pressure and heated from 230 K to 375 K and, subsequently, cooled back down to 235 K. The dotted lines between points are plotted as a visual guide. (b) The saturation pressures obtained for different coexistence temperatures. A second order polynomial fit is represented by the dotted lines. (c) The vapor-liquid surface tension at different temperatures. A linear fit is represented by the dotted lines.

than the boiling point and the condensation occurs for a supercooled fluid (the vertical dotted line in Fig. 9(a) marks the boiling point at 50 atm).

The boiling points at different pressures were also independently calculated using the same procedure in Ref. 30. Here, we study the liquid-vapor coexistence (with flat interface) of 13 500 atoms by placing the liquid domain at the center of a $8 \times 8 \times 25\,\text{nm}^3$ simulation box. The box size is fixed during the simulations and periodic boundaries are imposed in all three dimensions. The system is equilibrated to several temperatures. The data collection and averaging is done over 5 ns. Figure 9(b) shows the plot of the saturation pressure as a function of temperature. The curve is fit to a second order polynomial to obtain the boiling point at any desired pressure. At 20 atm pressure the boiling point is ∼243 K as marked in Fig. 9(b). The critical temperature of the fluid is also obtained to be 376.4 K, which is consistent with reported results.[31] Using Eqs. (2) and (3) in Ref. 30 we, then, calculate the Gibbs free energy difference between the two phases at different temperatures and pressures.

During the coexistence simulation we also monitor the normal and tangential pressure. The vapor-liquid surface tension is calculated using Eq. (1) in Ref. 30. Figure 9(c) shows the plot of the surface tension values for different temperatures. A linear fit is used to estimate the surface tension at 243 K to be 0.021 N/m. These Gibbs free energy and surface tension values may be compared with experimental values for argon. Since our model system has interaction parameters different from those describing argon, using thermodynamic equivalence of fluids described by LJ potentials we determine the 20 atm equivalent system pressure to be 5.7 atm.[32] The thermodynamic equivalence is established using reduced LJ units as follows:

$$T^* = \frac{k_B T}{\epsilon}, \tag{8}$$

$$P^* = \frac{P\sigma^3}{\epsilon}, \tag{9}$$

where k_B is the Boltzmann constant, T is the temperature, and P is the pressure. Energy, ϵ, and length, σ, parameters are chosen as 0.5758 kcal/mol and 0.3 nm for the model system. The corresponding values for argon are 0.2381 kcal/mol and 0.34 nm,[32] respectively. Upon comparing the obtained Gibbs free energy values with the experimental data reported for argon at the equivalent pressure,[33,34] slight differences are observed. The equivalent value for the surface tension from experiments is 0.024 N/m.[35] The differences can be attributed to the neglect of long-range pressure correction in the MD simulations.

C. Free energy analysis

To benchmark the free energy analysis for the LJ fluid around spherical NPs we first conduct simulations of fluid in contact with flat surface similar to what is reported in Ref. 30. For this purpose, we equilibrate the fluid to 20 atm and 200 K and then perform NEMD simulations by setting the planar solid substrate as the heat source and the center of the fluid as the heat sink. The solid slab has 500 atoms while the fluid domain consists of 17 000 atoms. This corresponds to a source-to-sink distance of ∼70 nm. Half of the fluid domain is shown in Fig. 10(a) and the sink location is also marked. In the NEMD simulation the sink temperature is fixed at 200 K and the solid temperature is gradually increased to 350 K to generate vapor phase near the substrate. Subsequently, the solid temperature is gradually decreased to obtain the condensation point. The condensation of the undersaturated vapor occurs at a solid temperature of 252 K. The temperature profile in half the fluid domain is shown in Fig. 10(b). Due to Kapitza resistance,[25] the corresponding surface fluid temperature is 248 K, which is higher than the boiling point at 20 atm pressure.

The density profile for the corresponding case is shown in Fig. 10(d). Near the surface an ordering of the liquid is seen similar to what is seen around low temperature spherical NPs (Fig. 2(b)). The normal pressure variation in the fluid for the same case is shown in Fig. 10(c). As expected from conditions of mechanical equilibrium the pressure normal to the solid surface remains constant within statistical error. Using the free energy values obtained at 20 atm pressure we compute the Gibbs free energy difference between the bulk liquid phase and the vapor phase of the LJ fluid, Δg. The spatial variation of Δg (units of kJ/kg) is plotted in Fig. 10(e). Any fluctuations seen are purely of statistical origin.

The local values of Δg are multiplied by the local density to calculate the local driving force for vaporization, ΔG (in units of energy per unit volume) in each planar bin. The integral of ΔG from the solid surface, Z_S, to the coordinate, Z_{SH}, at which superheated liquid reaches boiling temperature is used to estimate the total driving force towards vaporization (in units of J/m^2):

$$\Delta G_{tot} = \int_{Z_S}^{Z_{SH}} [\Delta G\, dz]. \tag{10}$$

The above estimate is based on the assumption that the non-equilibrium system in our simulations may be considered as a series of equilibrium systems at different local temperatures (and in general at different pressures).

In Fig. 11 we show plots of the density, normal pressure, temperature, and Δg profiles around a 10 Å NP maintained at 1000 K. From the pressure profile the wetting region, as discussed earlier, is evident. The low-density fluid can also be identified from the temperature profile (Fig. 11(c)) as discussed in reference to Fig. 4. Upon approaching the nanoparticle, Δg (see Fig. 11(d)) shows an increase due to temperature increase above the boiling point. Then the value drops slightly due to the pressure increase and associated boiling point increase. Finally, in the low-density fluid region the steep temperature rise dominates the behavior leading to a steep increase of the driving force. This is more so in the wetting region since the pressure averaged over the oscillations is essentially the same as the pressure at the edge of the wetting region. For local temperatures that exceed available free energy data we assume a linear variation of Gibbs free energy difference.

The integral of the ΔG from the particle surface, R_{NP}, to the radius, R_{SH}, at which superheated liquid reaches boiling

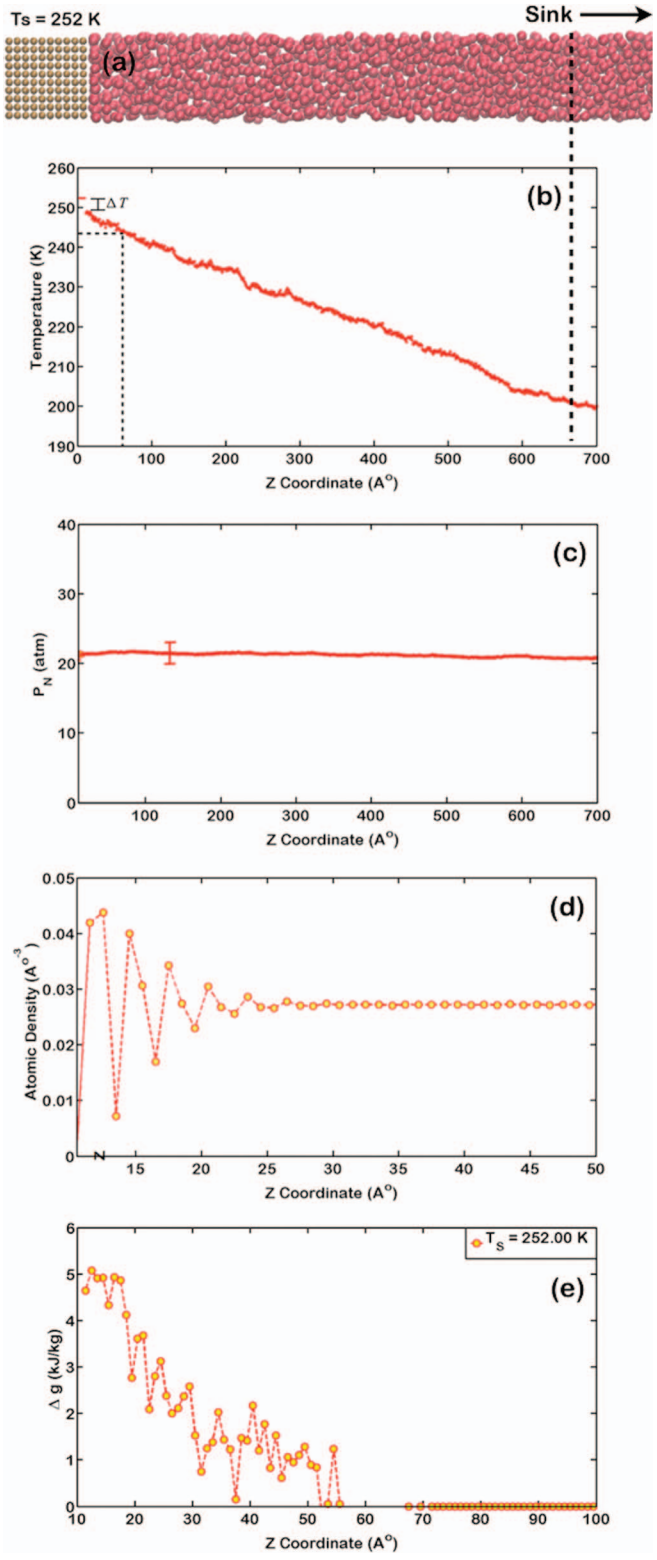

FIG. 10. (a) System schematic for fluid in contact with a hot flat substrate. The sink location is marked. Only half the fluid domain is shown. (b) Temperature profile in the fluid for a solid temperature of 252 K. A temperature drop at the interface between the solid and the liquid is seen. The temperature of the surface liquid is 248 K, which is greater than the boiling point at 20 atm pressure. The boiling point is marked out by the horizontal and vertical dotted lines. (c) The normal pressure in the fluid. Within statistical error the pressure is constant throughout. (d) The fluid density near the flat surface. Ordering is evident, which is a consequence of strong wetting. The dotted lines are plotted as a visual guide. (e) The driving force towards vaporization, Δg profile. Δg drops to zero for temperatures less than boiling. The dotted lines are plotted as a visual guide.

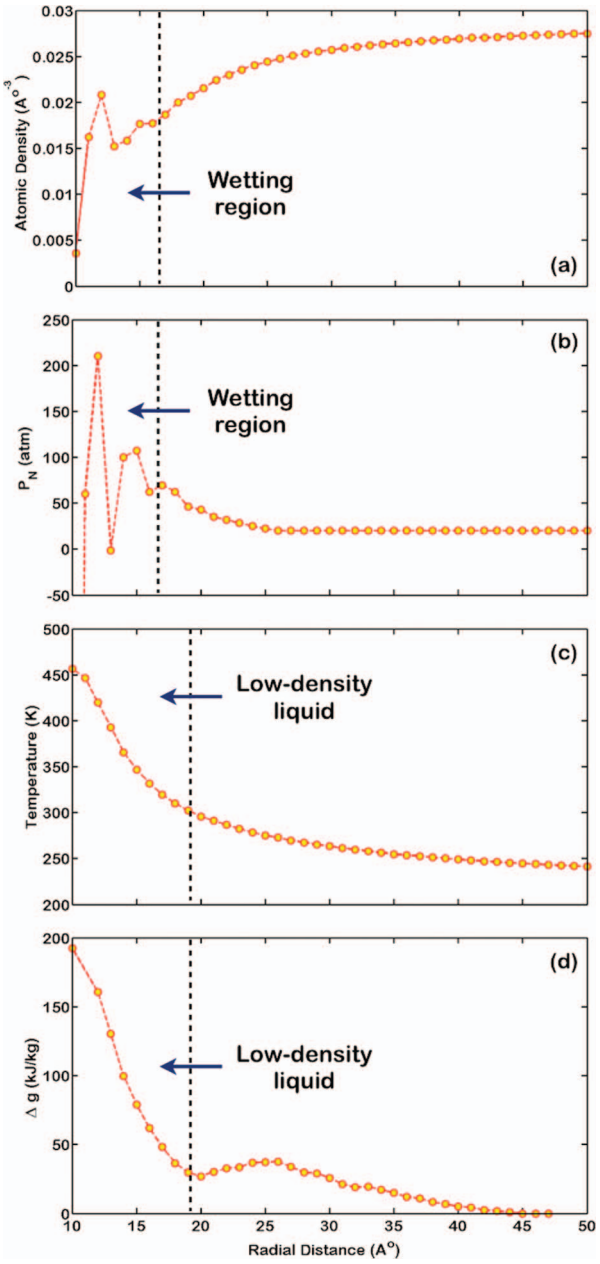

FIG. 11. (a) Sample density profile around a 10 Å nanoparticle that is maintained at 1000 K. (b), (c), and (d) show the corresponding spatial variation of the normal pressure component in spherically symmetric bins, the temperature profile, and Δg profile, respectively. We can identify the wetting and low-density fluid regions. The dotted lines between points are plotted as a visual guide.

temperature is used to estimate the total driving force towards vaporization (units of J):

$$\Delta G_{tot} = \int_{R_{NP}}^{R_{SH}} [4\pi r^2 \Delta G \, dr]. \tag{11}$$

We can now compare the driving force for vaporization with the vapor-liquid surface tension. As a limiting case we assume that there is always a liquid layer surrounding the nanoparticle surface, even at temperatures near the de-wetting limit. In our simulations we observe that vapor tends to form just outside the wetting region, hence, requiring the formation of two vapor-liquid surfaces. Such a phenomenon is described

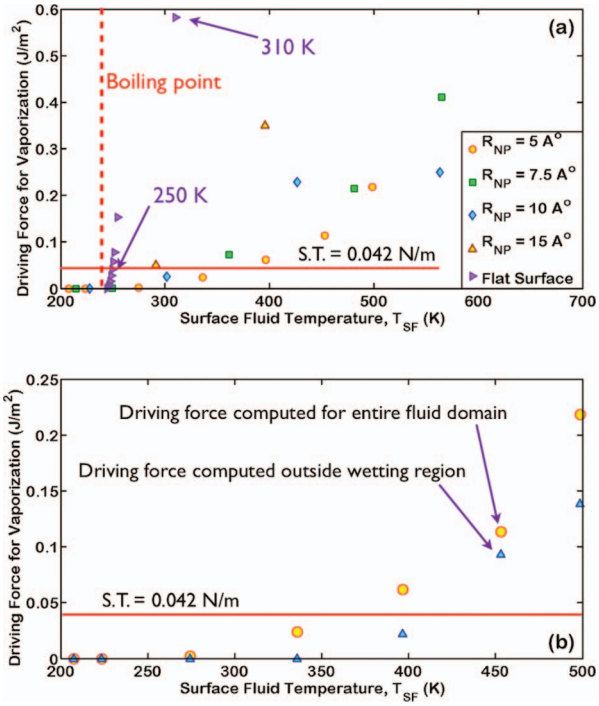

FIG. 12. (a) The driving force towards vaporization calculated using Eq. (11) is divided by the surface area of the wetting region. As a limiting case we assume that there is always a liquid layer attached to the nanoparticle surface. Hence, the formation of a vapor phase in a region slightly removed from the nanoparticle surface requires the formation of two vapor-liquid surfaces. We can compare the driving force per unit area with the total surface tension at the saturation conditions at 20 atm pressure. The total surface tension is represented as the solid line. For most of the above cases the driving force exceeds the surface tension. However, for the flat case the enhanced boiling point seen in the MD simulation is consistent with the point where driving force exceeds surface tension. This suggests that thermodynamically stable liquid can exist in non-equilibrium systems with temperature gradient even when local temperatures exceed the thermodynamic boiling point of the bulk fluid. However, such a simplistic model fails for severely non-equilibrium systems, such as those seen around intensely heated NPs. (b) For the 5 Å NP case driving forces computed over the entire fluid domain and outside the wetting region are compared. For both cases one sees that the total surface tension is exceeded for some cases.

in Ref. 36 where there is the presence of a liquid layer on a hot flat surface during the initial stages of phase transformation. This liquid layer is later seen to desorb. Thus, we divide ΔG_{tot} by the surface area of the wetting region to compute the driving force per unit area.

The surface area normalized ΔG_{tot} is plotted in Fig. 12(a) for different temperatures and the NP sizes that are below the critical size. These cases do not involve vaporization and one may expect that the driving force does not exceed surface tension. However, we see that for most of the cases the driving force exceeds the total surface tension of the two vapor-liquid surfaces. Since the inclusion of the wetting region in the driving force calculation might be questionable, we also compute the total driving force by only integrating Eq. (12) outside the wetting region. Both cases are compared in Fig. 12(b). The driving force is lowered but is still larger than the surface tension for several cases. This indicates that either the thermodynamic analysis presented here and the assumptions made lead to incorrect results, or that there is a significant barrier to the phase change which is kinetically suppressed.

To address the last question we turn our attention to the flat case results, which are also plotted in Fig. 12(a). The profiles obtained during the heating cycle are used in the analysis. In the MD simulation we see that beyond a surface fluid temperature of 310 K (the mechanical boiling point at 20 atm pressure) vaporization occurs near the solid substrate. The driving force for this limiting case can be seen to be several times larger than the total surface tension. In fact, the surface fluid temperature at which driving force equals surface tension is much lower and is equal to about 250 K. This temperature coincides with the MD observation for the condensation point where the system containing vapor at the flat interface was cooled down. This and the fact that the condensation process in our simulations does not involve nucleation, and associated barrier, demonstrate that the thermodynamic analysis is sound, but cannot be used as a stability criterion for vapor formation upon heating of NPs.

IV. SUMMARY AND CONCLUSION

In this work we use non-equilibrium molecular dynamics simulations to study the heat transfer characteristics surrounding an intensely heated nanoparticle immersed in a fluid. We focus our studies on the role of the nanoparticle curvature on the phase stability surrounding a simple Lennard-Jones liquid. We also perform a free energy analysis to validate the MD results. Our key findings are:

(1) Existence of local phase stability even at temperatures much above the mechanical boiling point is observed when fluid is in contact with a hot NP.
(2) Up to the critical particle size ($r = \sim 2$ nm in our model), the thermal flux saturates to a very high value as the particle temperature increases. Above the critical size, a phase change is observed, as is the case for a flat interface, and the thermal flux collapses.
(3) Two heat transfer regimes are observed for all cases. The temperature at which the regime change occurs depends linearly on the curvature and this is attributed, in part, to the balance between the Gibbs free energy decrease associated with the liquid-vapor transition and the surface tension of the liquid-vapor interface. However, this free energy model, while accurately describes the regime change near a flat surface upon condensation, fails to accurately capture the phenomenon around intensely heated NPs.

ACKNOWLEDGMENTS

This work is supported by the National Science Foundation (NSF) Grant No. 1033354. We would like to thank Meng Shen for useful discussions on the free energy analysis.

[1]D. G. Cahill, W. K. Ford, K. E. Goodson, G. D. Mahan, A. Majumdar, H. J. Maris, R. Merlin, and S. R. Phillpot, J. Appl. Phys. **93**, 793 (2003).
[2]Z. Wang, J. A. Carter, A. Lagutchev, Y. K. Koh, N. H. Seong, D. G. Cahill, and D. D. Dlott, Science (New York) **317**, 787 (2007).
[3]D. P. O'Neal, L. R. Hirsch, N. J. Halas, J. D. Payne, and J. L. West, Cancer Lett. **209**, 171 (2004).
[4]L. R. Hirsch, R. J. Stafford, J. A. Bankson, S. R. Sershen, B. Rivera, R. E. Price, J. D. Hazle, N. J. Halas, and J. L. West, Proc. Natl. Acad. Sci. U.S.A. **100**, 13549 (2003).

[5]N. Rozanova and J. Zhang, Sci. China Ser. B-Chem. **52**, 1559 (2009).
[6]D. O. Lapotko, E. Lukianova, and A. A. Oraevsky, Lasers Surg. Med. **38**, 631 (2006).
[7]M. Hu, P. Hristina, and G. V. Hartland, Chem. Phys. Lett. **391**, 220 (2004).
[8]A. Plech, V. Kotaidis, S. Grésillon, C. Dahmen, and G. von Plessen, Phys. Rev. B **70**, 195423 (2004).
[9]S. Merabia, S. Shenogin, L. Joly, P. Keblinski, and J. Barrat, Proc. Natl. Acad. Sci. U.S.A. **106**(36), 15113 (2009).
[10]S. Merabia, P. Keblinski, L. Joly, L. J. Lewis, and J. Barrat, Phys. Rev. E **79**, 021404 (2009).
[11]R. Lovett and M. Baus, J. Chem. Phys. **106**(2), 635 (1997).
[12]J.-P. Hansen and L. Verlet, Phys. Rev. **184**(1), 151 (1969).
[13]C. T. Avedisian, J. Phys. Chem. Ref. Data **14**(3), 695 (1985).
[14]J. E. Shepherd and B. Sturtevant, J. Fluid Mech. **121**, 379 (1982).
[15]D. M. Heyes, E. R. Smith, D. Dini, and T. A. Zaki, J. Chem. Phys. **135**, 124512 (2011).
[16]J. H. Irving and J. G. Kirkwood, J. Chem. Phys. **18**, 817 (1950).
[17]B. D. Todd, D. J. Evans, and P. J. Daivis, Phys. Rev. E **52**(2), 1627 (1995).
[18]F. Varnik, J. Baschnagel, and K. Binder, J. Chem. Phys. **113**, 4444 (2000).
[19]A. Harasima, Adv. Chem. Phys. **1**, 203 (1958).
[20]N. Baddour, J. Opt. Soc. Am. A **27**(10), 2144 (2010).
[21]N. Baddour, J. Opt. Soc. Am. A **26**(8), 1767 (2009).
[22]O. G. Jepps and S. K. Bhatia, Phys. Rev. E **67**, 041206 (2003).
[23]It is pertinent to note that the saturated vapor volume is ∼50 times the liquid volume for the MD system that is modeled here. However, due to the presence of a solid nanoparticle the overall system volume changes by only 10 times when vaporization occurs. The density values away from the nanoparticle stabilize at 0.0005 $Å^{-3}$, which is the saturated vapor density.
[24]I. U. Vakarelski, N. A. Patankar, J. O. Marston, D. Y. C. Chan, and S. T. Thoroddsen, Nature (London) **489**, 274 (2012).
[25]E. T. Schwartz and R. O. Pohl, Rev. Mod. Phys. **61**, 605 (1989).
[26]Z. B. Ge, D. G. Cahill, and P. V. Baun, Phys. Rev. Lett. **96**, 186101 (2006).
[27]Z. Liang, W. Evans, T. Desai, and P. Keblinski, App. Phys. Lett. **102**, 061907 (2013).
[28]Z. Liang, W. Evans, and P. Keblinski, Phys. Rev. E **87**, 022119 (2013).
[29]E. H. Kennard, *Kinetic Theory of Gases: With an Introduction to Statistical Mechanics* (McGraw-Hill Book Company Inc., 1983), pp. 61–63.
[30]Z. Liang, K. Sasikumar, and P. Keblinski, Phys. Rev. Lett. **111**(22), 225701 (2013).
[31]A. Trokhymchuk and J. Alejandre, J. Chem. Phys. **111**(18), 8510 (1999).
[32]C. Desgranges and J. Delhommelle, J. Chem. Phys **136**, 184107 (2012).
[33]W. C. Reynolds, *Thermodynamic Properties in SI: Graphs, Tables and Computational Equations for 40 Substances*, Dept. of Mechanical Engineering, Stanford University, 1979.
[34]N. B. Vargaftik, Y. K. Vinogradov, and V. S. Yargin, *Handbook of Physical Properties of Liquids and Gases* (Begell House, 1996), pp. 1022–1031.
[35]E. W. Lemmon and S. G. Penoncello, Adv. Cryo. Eng. **39**, 1927 (1994).
[36]Y. Dou, L. V. Zhigilei, N. Winograd, and B. J. Garrison, J. Phys. Chem. A **105**, 2748 (2001).